Quaternary Science Reviews 266 (2021) 107075

Contents lists available at ScienceDirect

Quaternary Science Reviews

journal homepage: www.elsevier.com/locate/quascirev

Hydroclimate variation during the Mystery Interval in the East Asian Summer Monsoon area

Bingyan Zhao [a, c, e], Xianyu Huang [b, f, *], Jianfang Hu [a, c, **], Junwu Shu [d], Weiming Wang [d], Ping'an Peng [a, c, e]

[a] State Key Laboratory of Organic Geochemistry, Guangzhou Institute of Geochemistry, Chinese Academy of Sciences, Guangzhou, 510640, China
[b] State Key Laboratory of Biogeology and Environmental Geology, China University of Geosciences, Wuhan, 430078, China
[c] CAS Center for Excellence in Deep Earth Science, Guangzhou, 510640, China
[d] State Key Laboratory of Palaeobiology and Stratigraphy, Nanjing Institute of Geology and Palaeontology, Chinese Academy of Sciences, Nanjing, 210008, China
[e] University of Chinese Academy of Sciences, Beijing, 100049, China
[f] Hubei Key Laboratory of Critical Zone Evolution, School of Geography and Information Engineering, China University of Geosciences, Wuhan, 430078, China

ARTICLE INFO

Article history:
Received 6 April 2021
Received in revised form
29 June 2021
Accepted 30 June 2021
Available online 9 July 2021

Handling Editor: P Rioual

Keywords:
Mystery Interval
EASM
Hydroclimate
Wetland sediment
Biomarker

ABSTRACT

The inconsistency of paleoclimate records between the mid-low and high latitudes during the Mystery Interval (MI, 17.5–14.5 ka BP) is not well resolved. To provide a mechanism analysis, this study conducts spatial comparisons of hydroclimate changes in the Asian Summer Monsoon (ASM) region during the MI by reconstructing the paleohydrology of the south of East Asian Summer Monsoon (EASM) region using the molecular distributions and carbon isotope ratio of *n*-alkanes, as well as elemental and isotopic composition of bulk organic matter, in a sedimentary core retrieved from Dingnan (DN) wetland. The multiple indices of the DN core confirmed the occurrence of dry-wet and wet-dry transitions at ca. 17.5 ka BP and 16.0 ka BP, respectively. Synchronous with the dry-wet transition in the DN records, the Indochina Peninsula at a slightly lower latitude became wetter. In contrast, the middle Yangtze region at a more northern latitude became slightly drier, and North China did not show a hydrological variation. Moreover, the wet-dry transition at the mid-MI was strong in the Indochina Peninsula (10–20°N, at about 16.5 ka BP) and the southern EASM region (23–27°N, at about 16.0 ka BP) but was nearly absent in the middle Yangtze region (28–32°N) and North China (35–40°N). The first hydrological transition possibly connects with the synchronous southward movement of the Intertropical Convergence Zone (ITCZ) and the westerly jet caused by the cooling of the Northern Hemisphere. The absence of the second hydrological transition is interpreted as a result of the decoupling of the ITCZ and the westerly jet caused by the delayed formation of the ITCZ due to the warming of the Southern Hemisphere. This study reveals spatial differences in the hydroclimate variations during the MI and highlights the potential influence of coupling between the westerly jet and the ITCZ on rainfall in the ASM region.

1. Introduction

The Mystery Interval (MI) occurred between 17.5 and 14.5 ka BP at the onset of the last deglaciation. During this period, global temperatures began to rise, and interactions between different climate systems intensified, resulting in a series of climate events that have been difficult to parse (Denton, 2006; Broecker and Putnam, 2012; Hodell et al., 2017). Investigations on the mechanisms of these climatic events can provide insights into the Earth's climate system and improve climate models and projections. During the MI, the North Atlantic Meridional Overturning Circulation (AMOC) slowed down (McManus et al., 2004), resulting in the North Atlantic region experiencing abnormally cold climates (Cacho et al., 2001). Meanwhile, surface sea temperatures (SST) in the Northern Hemisphere were lower than those in the Southern

* Corresponding author. State Key Laboratory of Biogeology and Environmental Geology, China University of Geosciences, Wuhan, 430078, China.
** Corresponding author. State Key Laboratory of Organic Geochemistry, Guangzhou Institute of Geochemistry, Chinese Academy of Sciences, Guangzhou, 510640, China.
E-mail addresses: xyhuang@cug.edu.cn (X. Huang), hujf@gig.ac.cn (J. Hu).

https://doi.org/10.1016/j.quascirev.2021.107075
0277-3791/

Hemisphere (Shakun et al., 2012). These events indicate that the ITCZ and the westerly jet may have shifted southward during the MI due to the change of temperature gradient between the Northern and Southern Hemispheres (Chiang and Friedman, 2012; Toggweiler, 2009). However, several records in the mid-low latitudes, where precipitation is sensitive to the mean position of the ITCZ and the westerly jet, capture the marked dry-wet and wet-dry turning points during the MI (Broecker and Putnam, 2012; Asmerom et al., 2017; McGee et al., 2018; Huang et al., 2019). These changes imply the possibility of repeated southward shifts of the ITCZ and the westerly jet during the MI. Therefore, a detailed reconstruction of the atmospheric activity in the mid-low latitudes during the MI might provide the key to reconcile the inconsistency between these records.

The Asian Summer Monsoon (ASM) region is one of the largest monsoon regions in the world. The rainfall in the north is mainly controlled by the westerly jet, and the rain in the south is primarily controlled by the ITCZ (Ding and Chan, 2005; Chiang et al., 2015; Zhang et al., 2018). Therefore, the change of climate and rainfall in this region can reflect changes in global atmospheric circulation. A close relation exists between atmospheric activity and local rain in the ASM region (Fig. 1; Ding and Chan, 2005). In the Indochina peninsula (10–20°N), the precipitation peak appears from March to April (Ding and Chan, 2005) due to the early seasonal formation of ITCZ in this region. In South China (23–27°N), the precipitation peak is from April to May, which results from the coupling between the enhancement of the westerly jet and increased delivery of water vapor from ITCZ carried by the southwest wind of the subtropical high (Wan et al., 2008, 2009). Controlled by the northward shift of the westerly jet, the precipitation peaks in Central China (28–32°N) and North China (35–40°N) appear in June–July and August, respectively (Chiang et al., 2015; Zhang et al., 2018). Therefore, reconstruction of the spatiotemporal pattern of hydrological conditions in the ASM region during the MI might improve our understanding of their formative mechanisms.

Rainfall variations during the MI in the southeastern shore of the Indochina Peninsula (Fig. 1; Huang et al., 2019; Li et al., 2019) and in the middle Yangtze region and North China have been well studied (Zhou et al., 2012; Zhang et al., 2018). In the Indochina Peninsula, rainfall increased at the initiation of the MI, and then it decreased near the end of the MI. In contrast, rainfall in the middle Yangtze region exhibited a slightly decreasing trend in the early MI and then maintained a wetter state until the end of MI. In North China, there was no hydrological variation during the MI (Zhou et al., 2012). However, well-dated paleohydrology records spanning the MI are absent in South China, an intermediate region

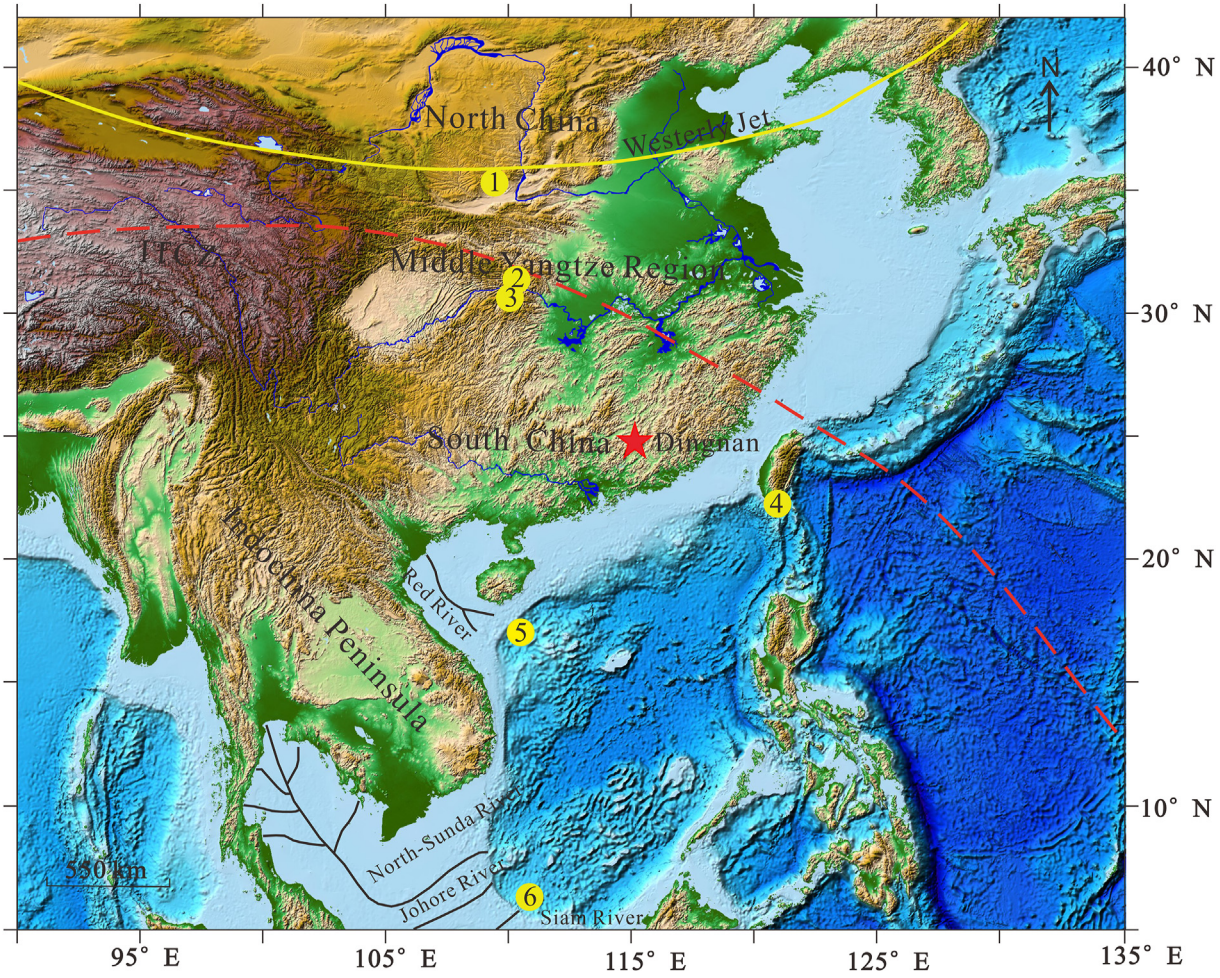

Fig. 1. Map of the research sites. The red star indicates the Dingnan wetland in this study. The Arabic numbers refer to the following locations: 1. Luochuan loess (Zhou et al., 2012), 2. Dajiuhu wetland (Zhao et al., 2018), 3. Haozhu cave (Zhang et al., 2018), 4. Dongyuan Lake (DYL, Ding et al., 2016), 5. PC338 core (Li et al., 2019), 6. CG2 (Huang et al., 2019). The red dashed line indicates the modern position of the ITCZ in July (modified from (Han et al., 2016). The solid yellow line indicates the modern position of the westerly jet in July. The topographic map was downloaded from https://ngdc.noaa.gov/mgg/global/relief/ETOPO1/image. (For interpretation of the references to color in this figure legend, the reader is referred to the Web version of this article.)

between the Indochina Peninsula and the middle and lower Yangtze region. This absence impedes inferring the spatial patterns of hydroclimate change during the MI and understanding their underlying mechanisms.

Wetland sediment sequences from South China are promising repositories of information on the hydrological evolution of the region during the MI. Sediment deposits in lake and wetland ecosystems, such as swamps and peatlands, can be linked with water level changes (Kratz and DeWitt, 1986; van der Valk, 2012). Elemental and isotopic composition of bulk organic matter, as well as the molecular distributions and stable carbon isotopic compositions of *n*-alkanes, provide powerful information to reconstruct past hydrological conditions and related ecological succession (Thorson and Webb, 1991; Newby et al., 2000; Almquist et al., 2001; Schellekens and Buurman, 2011; Street et al., 2013; Yamoah et al., 2016). The Dingnan wetland is located near the boundary of Guangdong and Jiangxi Provinces in South China (Fig. 1). Previous studies of the DN wetland revealed the alternation of peat and lake sediments from the Last Glacial Maximum to the late Holocene, indicating large hydroclimate changes (Zhou et al., 2004; Zheng et al., 2009; Zhong et al., 2015; Chen et al., 2020; Wei et al., 2020). However, due to the insufficient resolution and/or dating, the ambiguous proxies of the reconstruction of hydrological changes and the incomplete record of the MI, these records cannot provide detailed hydrological information during MI.

Here we present a new paleohydrological reconstruction for South China during the MI based on the distribution characteristics of *n*-alkanes, their carbon isotope ratios, and elemental and isotopic composition of bulk organic matter in a sediment core retrieved from the Dingnan wetland. This study fills a geographical gap between the Indochina Peninsula and the middle and lower Yangtze Region and contributes to a better understanding of hydrological variations in the ASM region during the MI.

2. Material and methods

2.1. Study site setting

The Dingnan wetland is located in the boundary between the watersheds of the Yangtze River and the Pearl River at the southern edge of the subtropical zone of China (Fig. 1). This area is strongly influenced by a monsoon climate and zonal climatic shifts (Zhou et al., 2004). The landscape around the Dingnan wetland has been strongly disturbed by human activities, and no native vegetation remains in its watershed today. However, natural vegetation found in a nearby nature reserve indicates that the original vegetation was dominated by evergreen broadleaf trees such as *Castanopsis*, *Lithocarpus,* and *Cyclobalanopsis* (Zhou et al., 2004). According to the meteorological data collected from 1981 to 2010 in the Dingnan Station, the annual mean temperature is 19.1 °C, and the annual mean precipitation is 1586 mm (Fig. 2a). The annual range of mean monthly temperature is 8.9–27.3 °C. The range of mean monthly rainfall is 50–254 mm, with a maximum occurring from April to June. The range of mean monthly relative humidity is 73–84%, which has a good correlation with the mean monthly rainfall ($R^2 = 0.81$, $p < 0.01$; Fig. S1). The Dingnan wetland was formed in an intermontane closed basin with impermeable igneous rock as the basement. Therefore, the internal water level of the wetland is mainly controlled by the balance between rainfall and evaporation.

2.2. Core sampling and chronology

A sediment core (DN-1, N24°45′24.3″, E115°02′11.7″, altitude 267 m) was retrieved from the southern part of the Dingnan wetland in November 2011 using a gravity corer (Fig. 2b). As shown in Fig. 3, the bottom layer consists of interbedded light-yellow gravel and clay (6.71–7.36 m), which is overlain by alternations of black peats and grey/black mud and gravels (6.71–1.17 m), followed by light-yellow sand and interbedded brown sand and clay (1.17–0.29 m), and finally covered by a brown soil layer (0–0.29 m).

The core was transported to the State Key Laboratory of Palaeobiology and Stratigraphy (Nanjing, China) as quickly as possible and then sliced at 1-cm intervals and stored at −20 °C until analysis. Twelve samples, including bulk sediments and terrestrial plant macrofossils from different depths, were selected and sent to the Beta AMS Lab, Miami, USA, for accelerator mass spectrometry (AMS) ^{14}C analysis (Table 1). The age-depth model of the core was constructed by using Bacon 2.5.2 package (Blaauw and Christen, 2011) based on the R software (v4.0.2; R Core Team, 2020).

2.3. Bulk geochemical analyses

Sediment samples were freeze-dried, homogenized, and powdered. A portion of each sample was treated with 6 N HCl for 24 h at room temperature to remove carbonate and then rinsed with deionized water (Hu et al., 2006). The carbonate-free samples were dried and then were analyzed for the total organic carbon (TOC) and total nitrogen (TN) content on a Thermo electron FLASH EA 1200 Series CNS elemental analyzer. Duplicate analyses were performed for every sample, with the mean of the two measurements reported in this study. Replicate analysis of one sample ($n = 5$) gave a 1σ precision of ±0.02 wt %C and ±0.003 wt %N. The precision of the duplicated C/N ratios was better than ±2.8.

Analysis of the carbon isotope ratio of bulk organic matter was performed on carbonate-free sediment samples using a FLASH 2000 Elemental Analyzer connected to a Thermo MAT-253 isotope ratio mass spectrometer. Results are reported as the δ notation in per mil (‰) relative to the Vienna Peedee Belemnite (VPDB) standard. Analytical precision for international and in-house reference materials was almost always better than ±0.2‰ ($n = 5$). Replicate measurements of samples yielded similar standard deviations, less than ±0.3‰.

2.4. Lipid analyses

About 15 g of powdered sample was ultrasonically extracted with a solvent mixture of dichloromethane and methanol (CH_2Cl_2/CH_3OH, 9:1, v/v) and repeated at least six times until no noticeable color was observed in the supernatant. Activated pure copper was added to the lipid extracts overnight to remove elemental sulfur. The total extract was then concentrated with a rotary evaporator and then separated by silica column chromatography to obtain saturated hydrocarbons by eluting *n*-hexane. The flash column was prepared by filling a glass column (10 cm × 1 cm i. d) with silica gel, which was previously extracted for 72 h and then activated at 150 °C for 2 h.

The concentration of saturated hydrocarbons was determined on a HP 6890 gas chromatograph (GC) equipped with an flame ionization detector (FID) and a 30 m DB-5MS fused capillary column (i.d. 0.25 mm; 0.25 μm film thickness). Nitrogen was used as the carrier gas. The oven temperature was programmed to increase from 80 °C (holding for 2 min) to 200 °C at a rate of 10 °C/min and then increased to 290 °C (holding for 25 min) at a rate of 4 °C/min. The C_{36} alkane was used as an internal standard. One working standard sample was inserted between every 10 samples to ensure that the precision of ACL, CPI and P_{aq} values were better than ±0.1, ±0.1 and ± 0.01, respectively. After GC analyses, the saturated hydrocarbon fraction was purified for *n*-alkanes using urea adduction (Xie et al., 2007).

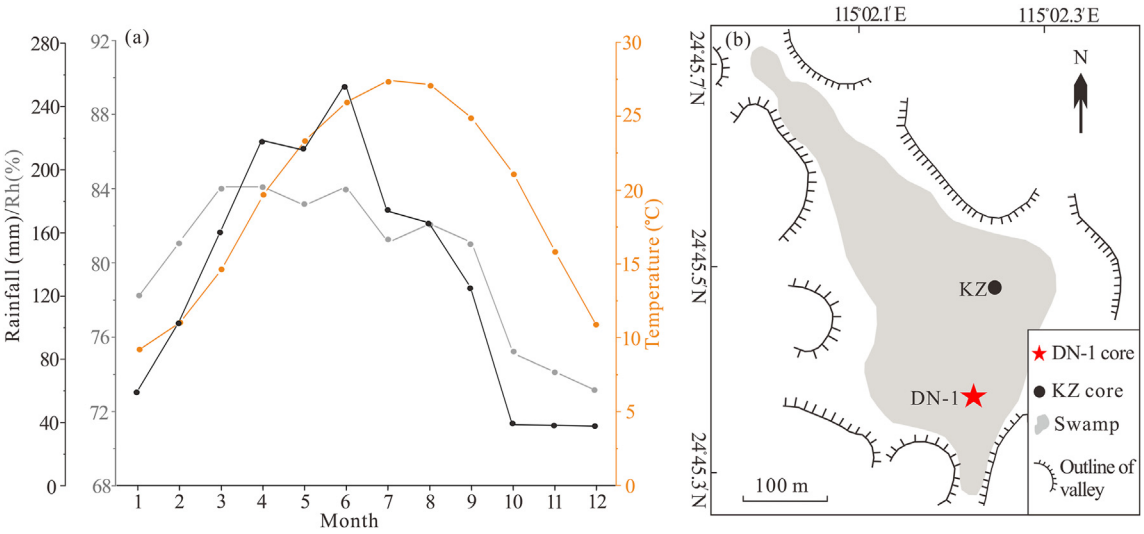

Fig. 2. The mean monthly meteorological information and topographic diagram of the study site (Zhou et al., 2005). (a) The seasonal variation of mean monthly average rainfall, air temperature, and relative humidity (RH). (b) The star presents the study site.

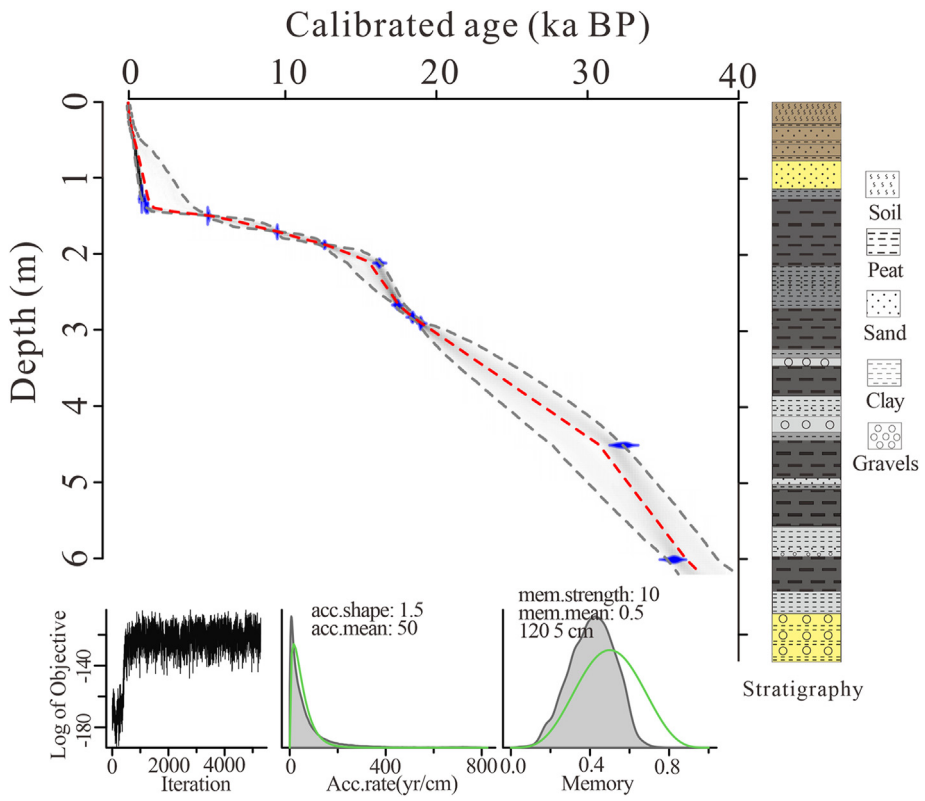

Fig. 3. Chronology and lithology of the DN-1 core. The red line represents weighted mean ages for each depth based on the Bayesian depth-age model (Blaauw and Christen, 2011). (For interpretation of the references to color in this figure legend, the reader is referred to the Web version of this article.)

The $\delta^{13}C$ values of *n*-alkanes were measured using an Isoprime GC-isotope ratio mass spectrometer (GC-IRMS) with an HP-5 MS fused capillary column (60 m × 0.25 mm i. d.; 0.25 μm film thickness). The injector was used in splitless mode at 290 °C; helium was the carrier gas. The oven temperature was programmed as same as the above GC temperature program. To check the instrumental performance, *n*-alkane mixtures from Indiana University with known $\delta^{13}C$ values were measured every ten injections. All samples, reported in per mil (‰) versus Vienna Peedee belemnite (VPDB), were run at least in duplicate, with an average standard deviation of <0.5‰.

3. Results

3.1. Chronology

The radiocarbon ages were calibrated against the IntCal13 Northern Hemisphere calibration curve (Reimer et al., 2013) and

Table 1
Details of the AMS^{14}C dating and calibrating results with OxCal 7.0.4 (IntCal13 data set) for the DN-1 core.

Sample No.	Depth (cm)	Material	AMS^{14}C (a BP±1σ)	Calibrated age (cal. a BP)
DN1 128-129	128.5	twigs	430 ± 30	452–529
DN1 133-134	133.5	twigs	820 ± 30	686–784
DN1 140-141	140.5	twigs	930 ± 30	786–924
DN1 150-151	150.5	twigs	4330 ± 30	4843–4967
DN1 171-172	171.5	bulk peat	8430 ± 40	9401–9529
DN1 188-189	188.5	bulk peat	10,610 ± 50	12,522-12702
DN1 212-213	212.5	bulk peat	13,480 ± 60	16,013-16470
DN1 267-268	267.5	twigs	14,300 ± 50	17,211-17604
DN1 283-284	283.5	twigs	15,160 ± 50	18,272-18591
DN1 291-292	291.5	bulk peat	15,740 ± 50	18,854-19147
DN1 451-452	451.5	bulk peat	28,440 ± 170	31,714-32956
DN1 601-602	601.5	bulk peat	31,820 ± 230	35,166-36220

expressed in years before present (BP), where 'present' is defined as 1950 CE (Table 1). According to the fitting result of the Bacon programming, the 6-m sedimentary sequence spans over 36 ka (Fig. 3).

During the period of 20.0–11.0 ka BP, there were five dating points, 4 of which evenly covered 19.0–16.2 ka BP, providing a reasonable constraint on the starting time of MI (Fig. 4a). The 95% confidence ranges at 17.5 ka BP and 16.0 ka BP in the age-depth model were 17.9–17.3 ka BP and 16.5–14.5 ka BP, respectively (Fig. 3). To validate the accuracy of the timing of the mid-late MI in the DN-1 core, the TOC values sorted according to the depth-age model were compared with those of a nearby core (named KZ core). The TOC values of the two cores both show about 16.0 ka BP as the turning point for jumping from low to high values (Zhou et al., 2004; Yu et al., 2020). Moreover, uniform coverage of 16.7–14.6 ka BP by three radiocarbon dates in the KZ core provides a reasonable constraint on the time series of the mid-late MI (Fig. 4a and b).

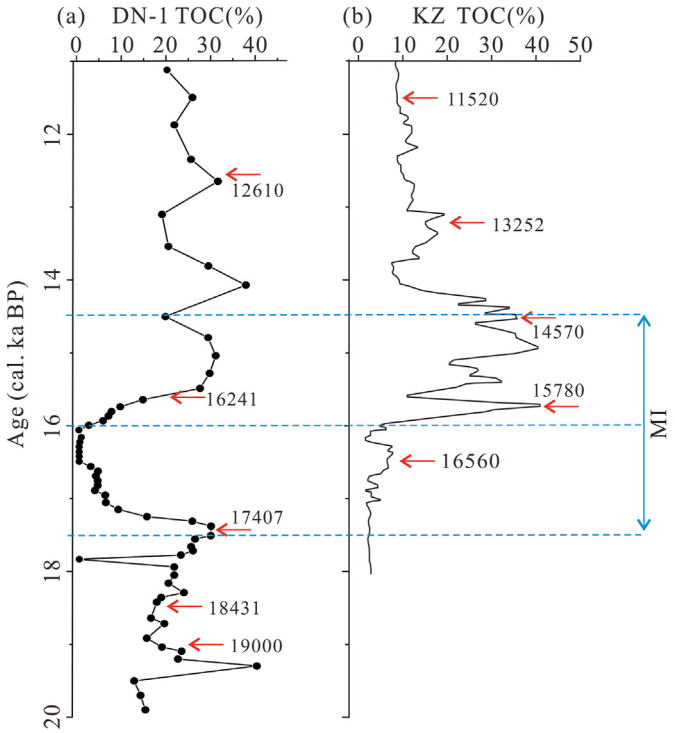

Fig. 4. Variations of TOC content. (a) TOC of DN-1 core. (b) TOC of KZ core (Zhou et al., 2005). The age data is the median of the calendar age.

3.2. Bulk geochemical results

The value ranges of TOC, C/N atomic ratio, and the $\delta^{13}C$ of bulk organic matter ($\delta^{13}C_{org}$) are 0.4–37.8%, 28.1–50.5, and −28.6–26.4‰, respectively (Fig. 5a, b, c). Before the MI (20–17.5 ka BP), the TOC concentration showed an increasing trend from 15.3% to 29.9%, except for the abnormally low and high values at ca. 17.8 ka BP and 19.3 ka BP. The C/N ratio is stable between 28.1 and 40.0 during 20–17.5 ka BP, except for the relatively high values at ca. 19.3 ka BP and 17.8 ka BP. The $\delta^{13}C_{org}$ values fluctuate between −27.8‰ and −28.6‰ during 20–17.5 ka BP. During the MI, the TOC concentration drops rapidly from 30% to 5% at around 17.5

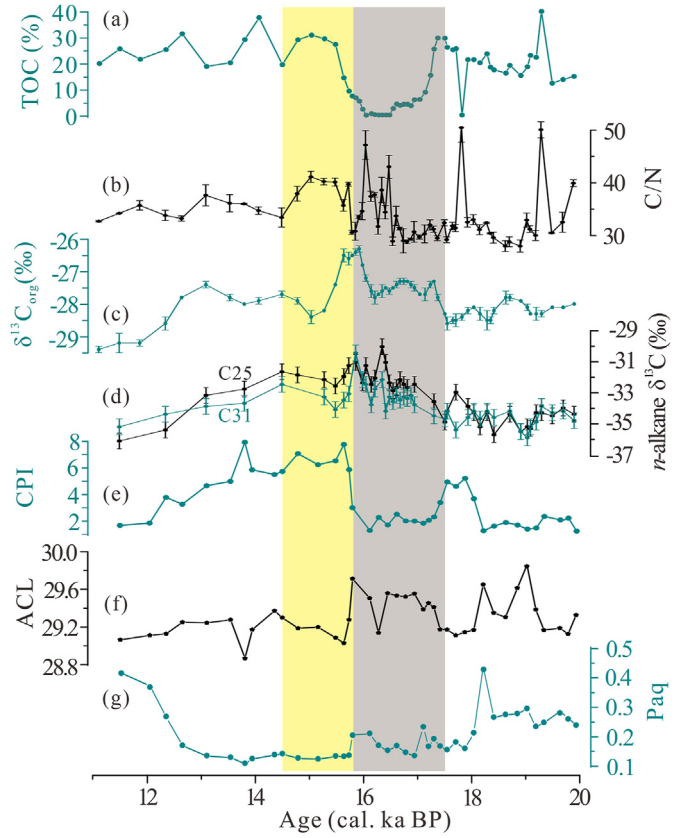

Fig. 5. Down core profiles of multiple indices of the DN-1 Core. (a) TOC, (b) C/N, $\delta^{13}C$ of bulk organic matter (c) and the C_{25} and C_{31} *n*-alkanes (d), (e) CPI, (f) ACL, (g) P_{aq}. Brown shades indicate wet periods, while the yellow shade indicates the drier period. (For interpretation of the references to color in this figure legend, the reader is referred to the Web version of this article.)

ka BP, reaches the lowest values of 0.4% around 16.5–16.0 ka BP, and then rapidly rises to 30%. C/N atomic ratios remain relatively stable around 29.0–33.8 during 17.5–16.5 ka BP, then fluctuate between 31.8 and 47.2 at 16.5–16.0 ka BP, and finally remain relatively stable (>30) from 16.0–14.5 ka BP. The $\delta^{13}C_{org}$ values rise rapidly from −28.5‰ to −27.5‰ around 17.5 ka BP, increase to −26.5‰ during the several hundred years after 16.0 ka BP, and then quickly decrease to −28.5‰ at 15.5 ka BP. After the MI, the TOC concentrations are relatively stable, fluctuating between 19.1% and 37.8%. The C/N ratio is also stable, ranging from 32.8 to 37.7. The $\delta^{13}C_{org}$ first stabilizes between −27.4‰ and −28.0‰, and then gradually decreases to −29.4‰ after 13 ka BP.

3.3. Molecular distributions and carbon isotope compositions of n-alkanes

The carbon numbers of the *n*-alkane for all the analyzed sediments range from C_{14} to C_{33}, and the long-chain alkanes beyond C_{23} show a significant odd carbon preference. The molecular distribution patterns were assessed with the carbon preference index (CPI), the average chain length (ACL), and the aquatic plant *n*-alkane proxy (P_{aq}). The CPI, ACL, and P_{aq} were calculated as follows (Marzi et al., 1993; Ficken et al., 2000; Freeman and Pancost, 2014):

$$CPI = \frac{1}{2} \times \left(\frac{C_{23}+C_{25}+C_{27}+C_{29}+C_{31}}{C_{24}+C_{26}+C_{28}+C_{30}+C_{32}} + \frac{C_{25}+C_{27}+C_{29}+C_{31}+C_{33}}{C_{24}+C_{26}+C_{28}+C_{30}+C_{32}}\right)$$

$$ACL=(27\times C_{27}+29\times C_{29}+31\times C_{31}+33\times C_{33})/(C_{27}+C_{29}+C_{31}+C_{33}).$$

$$P_{aq}=(C_{23}+C_{25})/(C_{23}+C_{25}+C_{29}+C_{31}).$$

The ranges of CPI, ACL, and P_{aq} values are 2.7–9.4, 28.9–29.9, and 0.15–0.45, respectively (Fig. 5e–g). During 20.0–16.0 ka BP, the CPI values remain around 3 from 20 to 16 ka with a peak to 5 at around 18.0–17.5 ka BP (Fig. 5e). The ACL exhibits two increases up to 29.6 around 19.0–18.0 ka BP and 17.5–16.0 ka BP (Fig. 5f). The P_{aq} values decrease from about 0.30 to about 0.20 at 18 ka BP (Fig. 5g). From 16.0 to 11.0 ka BP, the CPI values sharply rise to 9.3 after at 16.0 ka BP and decrease thereafter (Fig. 5e). The ACL shows lower values varying between 28.9 and 29.4 (Fig. 5f). The P_{aq} values are about 0.10 after 16.0 ka BP and sharply rise to 0.42 after 13.0 ka BP (Fig. 5g).

To better distinguish the input contributions of aquatic and terrestrial plants from the carbon isotope ratios of *n*-alkanes, this paper focuses on the carbon isotope composition of the C_{25} and the C_{31} *n*-alkanes, which are each respectively sourced mainly from aquatic plants and higher terrestrial plants (Ficken et al., 2000; Bi et al., 2005; Bush and Mcinerney, 2013; Zhao et al., 2018). The $\delta^{13}C$ of *n*-C_{25} ($\delta^{13}C_{25}$) and *n*-C_{31} ($\delta^{13}C_{31}$) are between −36.0‰ and −30.0‰ and from −35.8‰ to −30.4‰, respectively, and exhibit a similar trend (Fig. 5d). In the periods before the MI (20–17.5 ka BP), the $\delta^{13}C_{25}$ and $\delta^{13}C_{31}$ have almost the same relatively negative values, ranging from −35.8 to −32.9‰. During the MI, their values are less negative than those of the adjacent periods, attaining increases of 2–5‰, especially the $\delta^{13}C_{25}$. In the latter stage of the first half of the MI (16.5–16 ka BP), the $\delta^{13}C_{25}$ and $\delta^{13}C_{31}$ both reach their least negative values. In the periods after the MI, the $\delta^{13}C_{25}$ and $\delta^{13}C_{31}$ values decrease from −31.6‰ to −36.0‰ and from −32.4‰ to −35.1‰, respectively, and show an offset of about 1.4‰.

4. Discussion

4.1. Paleoclimate reconstruction during the MI from the Dingnan wetland

4.1.1. Hydroclimate variations during the MI

In lacustrine and peat deposits, the sedimentary TOC values mainly reflect the balance between productivity and degradation (Meyers and Ishiwatari, 1993; Meyers, 2003). In peatlands, the waterlogged and anaerobic conditions facilitate the production and accumulation of *in situ* plant organic matter and consequently results in high TOC concentrations, which can reach 50% or higher (Chambers et al., 2012; Loisel et al., 2014). In lakes, low *in situ* productivity and a relatively high degradation rate lead to lower sedimentary TOC (TOC <10%) (Meyers and Ishiwatari, 1993). For example, the TOC values in the surface samples are almost all <2% in the shallow freshwater lakes in the middle and lower Yangtze region (Dong et al., 2012).

In the DN-1 core, TOC decreases at the beginning of the MI, around 17.5 ka BP, and reaches the lowest values during 16.4–16.0 ka BP (Fig. 5a). Correspondingly, the lithology changes gradually from peat to clay, and then sand particles with uniform grain size in clay increase gradually (Fig. S2). The coupling between TOC and lithology may indicate that a rise of water level in the peatland led to the deposition of organic-poor clay, and then the expansion of the water body inundated the swamp, and therefore sand carried by runoff could directly enter the swamp (Fig. 4a). The lacustrine deposit overlying the peat deposit is opposite to the natural evolution process of peatlands. This feature may be because Dingnan wetland formed in a closed intermontane depression, which would accumulate water to form a lake under periods with enhanced rainfall and therefore develop lacustrine deposits. Considering the lower temperature during the MI (Peterse et al., 2011; Opitz et al., 2015; Chu et al., 2017), the reduced evaporation may also contribute to the rise of water level. Therefore, this sequence is in large part a record of a climatic rainfall event. During the latter half of the MI, TOC in the DN-1 core increased rapidly at around 16.0 ka BP and then remained at high and stable values. Concurrently, the TOC of the nearby KZ core also increased rapidly and remained stable values, implying a record of consistent signals across the basin (Fig. 4a and b; Zhou et al., 2004). This pattern could be attributed to a relatively dry climate promoting the transformation of a lake back to a peatland. This phenomenon of intense rainfall leading to the development of lacustrine facies and followed by relatively dry climate promoting the re-establishment of a peatland is also found in the sedimentary record of a nearby intermountain depression (Ma et al., 2016). Therefore, the TOC of DN-1 reveals a wet climate transition at around 17.5 ka BP, and a dry climate transition at about 16.0 ka BP.

CPI is a proxy used to assess the odd-over-even ratio of carbon chain lengths of long-chain *n*-alkanes (Bray and Evans, 1961). The CPI values are mediated by plant source and sedimentary environmental conditions. In current conditions, the CPI values of 81% terrestrial higher plants range between 2 and 99, which are larger than those of 2.5–4.0 in algae and 1–2 in microorganisms (Bush and Mcinerney, 2013; Chen et al., 2020; Massa et al., 2021). During early diagenesis, the CPI signals are commonly smoothed by microbial activities under the influences of temperature and humidity (Xie et al., 2004; Huang et al., 2016; Naafs et al., 2019).

During the lacustrine stage of 17.5–16.0 ka BP (Fig. 5a; 6e), the CPI values in the DN-1 core are relatively low (2.5–4) but still higher than the values typical of algae and bacteria-derived *n*-alkanes. In the nearby Dajiuhu peatland (31°28′N, 110°00′E), also in the subtropic region, the CPI values in peat-forming plants are significantly higher in herbaceous plants than those of shrubs,

aquatic plants, and ferns (Zhao et al., 2018). Compared to lake settings, the waterlogged and anaerobic conditions in peatlands would exert relatively strong inhabitation on microbial degradation of *n*-alkanes and result in relatively higher CPI values in peat layers (Chambers et al., 2012; Loisel et al., 2014). It seems strange that the peat layer deposited before the MI displays low CPI values similar to those of the lacustrine deposition during the MI. Such reduced CPI values might be related to water level stability, the influences of drought, or the flourishing of woody plants. In addition, long-term anaerobic peat decomposition would decrease the CPI values in peat layers with longer burial histories.

The CPI values in the DN-1 core exhibit a change around 16.0 ka BP from low values in the early MI to high values in the late MI. This change is not consistent with the vegetation change from herbaceous plants to woody plants during the last deglaciation revealed by the pollen results in the KZ core (Zhou et al., 2004). Paleotemperature records show that the air temperature in the EASM during the MI may be affected by North Atlantic cooling events, showing an overall low temperature, or it may be synchronous with the rise of the North Hemisphere summer insolation, showing a rapid warming trend (Peterse et al., 2011; Opitz et al., 2015; Chu et al., 2017). Obviously, the two air temperature trends are not consistent with the trend of CPI values in the DN-1 core. According to current meteorological data, the seasonal variation of rainfall amount in the Dingnan area is greater than that of air temperature (Fig. 2a). As a result, the atmospheric humidity in this area is mainly controlled by rainfall (Fig. 2a). This phenomenon might make rainfall more important than temperature in affecting microbial degradation. However, the decreased humidity does not favor the increase of CPI values at 16.0 ka BP. During the transition from lake to peat sediments, the decrease in moisture allowed the transition back to a peatland, but the water table was still high enough to preserve peat, and hence maintained relatively high CPI values at 16.0 ka BP.

The ACL value of *n*-alkane distributions is affected by plant types and environmental conditions (Tipple and Pagani, 2013; Bush and Mcinerney, 2013). Numerous studies have found that the ACL values of plants are higher under relatively high temperature and drought conditions (Diefendorf and Freimuth, 2017). The ACL values in the DN-1 core exhibit the highest values in sediments deposited from 17.5–16.0 ka BP (Fig. 5f) when the lacustrine setting developed and the climate was cold (Peterse et al., 2011; Opitz et al., 2015; Chu et al., 2017). Therefore, the ACL in the DN-1 mainly reflects vegetation transition from herbaceous plants to woody plants during the MI. Although this is consistent with the pollen variation in the KZ core (Zhou et al., 2004), the relative percentage of woody plants indicated by pollen increased from 40% to 80%, and the variation range of ACL was only 0.4.

P_{aq} could be used to reflect the input of submersed plants and *Sphagnum* in wetland sediments (Ficken et al., 2000; Nichols et al., 2006). The P_{aq} values in the DN-1 core vary in a relatively narrow and low range (0.12–0.23) during the MI (Fig. 5g), although there are changes of lacustrine and peat facies (Fig. S2). Collectively, the significances of ACL and P_{aq} in the DN-1 core are ambiguous for their small variation ranges. This behavior might be caused by an overlap of *n*-alkane distributions from different plant groups (Bush and Mcinerney, 2013; Zhao et al., 2018).

4.1.2. Responses of plants to hydroclimate variations

The $\delta^{13}C$ of plant organic matter can reflect the photosynthetic pathways, such as C_3 and C_4 plants (Farquhar et al., 1989), the photosynthetic productivity that is controlled by the temperature (Wang et al., 2013; Jia et al., 2015), and also the ratio of aquatic to terrestrial plant input (Chikaraishi and Naraoka, 2003). In wetter conditions like in the Dingnan wetland, C_3 plants predominate over C_4 plants. This dominance was confirmed by the range of $\delta^{13}C_{org}$ values (from −28.6 to −26.4‰) and the absence of C_4 plant-derived pollen in the near KZ core (Zhou et al., 2004). Thus, the influence of C_4 plants in the $\delta^{13}C$ values is not considered here. In terms of the influence of vegetation types, the positive excursion of $\delta^{13}C$ of organic matter in lakes could be found to reflect the higher input of submerged plants or algae, which mainly use ^{13}C-enriched HCO_3^- as the carbon source (Mook et al., 1974; Yamoah et al., 2016). Moreover, the values of $\delta^{13}C_{org}$, $\delta^{13}C_{25}$, and $\delta^{13}C_{31}$ of the DN-1 core exhibit an increasing trend in the early MI (Fig. 5c and d), corresponding to the development of lacustrine facies and the included occurrence of the sand layers (Fig. S2). In particular, the C_{25} *n*-alkane, which mainly comes from aquatic plants (Ficken et al., 2000), has larger $\delta^{13}C$ values than those of the C_{31} *n*-alkane in the DN-1 core (Fig. 5d). The pollen records of the adjacent KZ core also verified the existence of aquatic plants during this period (Zhou et al., 2004). During the last stage of the MI, the stable offset between $\delta^{13}C_{25}$ and $\delta^{13}C_{31}$ is consistent with the characteristics of woody plants in the Dajiuhu peatland (Zhao et al., 2018). The development of woody plants during the last stage of the MI is also supported by the C/N ratio and pollen results (see the following discussion). Therefore, during the MI, the characteristics of carbon isotope compositions indicate a gradually increasing input of aquatic plants and then the dominance of woody plants, revealing the gradual expansion and then rapid regression of the water body.

The C/N atomic ratio is usually an effective indicator of terrestrial input in lake sediments (Hedges and Oades, 1997; Meyers and Lallier-Vergès, 1999; Meyers, 2003). The atomic C/N ratios of phytoplankton and heterotrophic bacteria are 6–10 and 4–8, respectively. Terrestrial higher plants have higher C/N atomic ratios ranging from 10 to 130 in their tissues, of which woody plants have the largest C/N ratios ranging from 175 to 400 owing to their high lignin and tannin content. However, aquatic macrophytes also have larger C/N atomic ratios overlapping with terrestrial plants (Finlay and Kendall, 2007). During 17.0–16.5 ka BP, the relatively low C/N atomic ratios, coupling the lacustrine facies revealed by the lithology and the relatively high $\delta^{13}C_{org}$ values, suggest the inputs of macrophytes or algae. During 16.5–16.0 ka BP, the C/N atomic ratios suddenly increase and fluctuate widely. At the same time, the sand layers frequently appeared (Fig. S2). This might be due to frequent heavy rainfall increasing the wash-in of sand and wood debris. After 16.0 ka BP, the higher C/N atomic ratios may reflect the flourishing of woody plants under relative drying conditions. This is consistent with the increase of tree pollen proportion from 40% to 80% in the palynological study of the KZ core (Zhou et al., 2004).

Moreover, an investigation of the adjacent peatlands found that woody plants are widely developed in the higher elevation areas (Zhao et al., 2018). In addition, a recent study has shown that woody litter could leach polyphenolics and consequently inhibit microbial degradation of organic matter (Fenner and Freeman, 2020). Thus, the C/N atomic ratios of the DN-1 core reveal the abundance of woody plants and consequently confirm drying conditions as also implied by the other indices at around 16.0 ka BP.

4.2. Mechanisms of paleohydrological variation during the MI in the ASM region

Collectively, the DN-1 records indicate the local climate became wetter at 17.5 ka BP and then turned rapidly to drier at 16.0 ka BP, which is reflected in the transition from herbaceous peat to lacustrine sediment to woody peat (Fig. 6c and d). The sudden drying at about 16.0 ka BP is supported by variations of CPI, TOC and palynology in the nearby KZ core (Zhou et al., 2004, 2005). The evolution of hydroclimate during the MI in the DN-1 core is consistent with records from other sedimentary sequences from

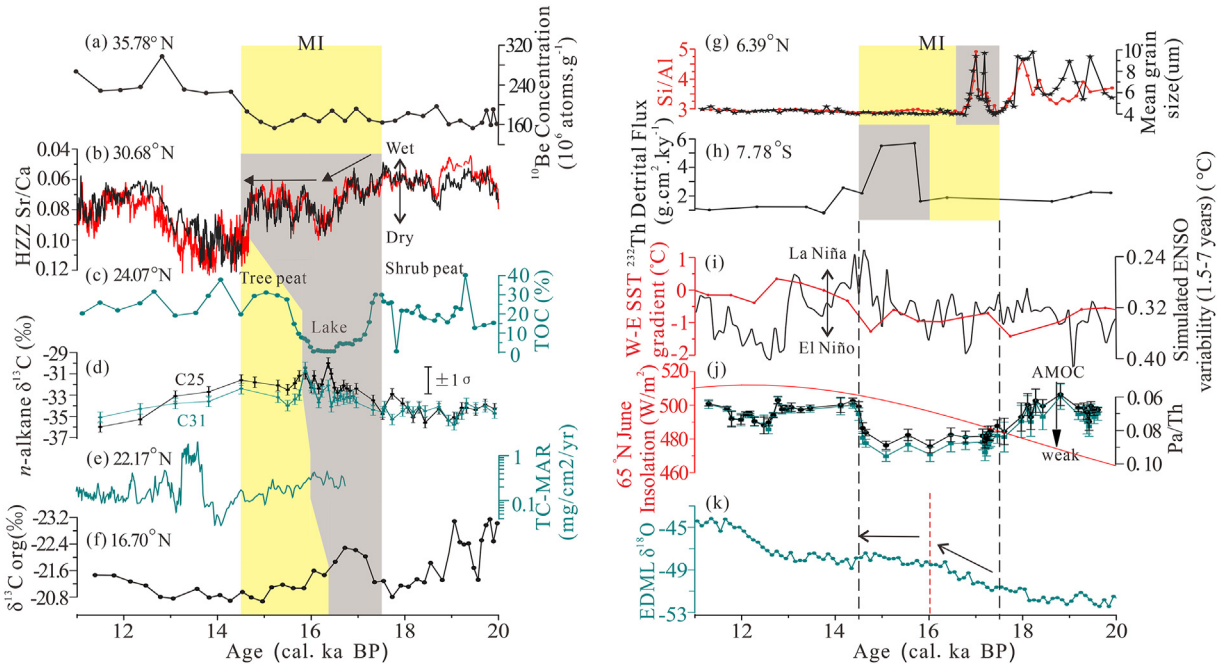

Fig. 6. Comparisons of paleoclimate records. (a) Loess ^{10}Be record in North China (Zhou et al., 2012). (b) Stalagmite Sr/Ca time series of Haozhu cave ("HZZ PC1") (Zhang et al., 2018). (c), (d) TOC values and δ^{13}C of the C_{25} and C_{31} *n*-alkanes of DN-1 core (this study). (e) Mass accumulation rate of TC of DYL core (Ding et al., 2016). (f) The δ^{13}C of the bulk organic matter of PC338 core (Li et al., 2019). (g) The mean grain size and Si/Al of the CG2 core (Huang et al., 2019). (h) Detrital fluxes of ^{232}Th in the Western Pacific Warm Pool (Muller et al., 2012). (i) The west-east Pacific Sea Surface Temperature (SST) gradient (Koutavas and Joanides, 2012) and simulated ENSO variability (Liu et al., 2014). (j) The 65° N July summer solar insolation (Laskar et al., 2004) and the North Atlantic sediment core GGC5 ^{231}Pa/^{230}Th (proxy of AMOC) (McManus et al., 2004); (k) The Antarctic EDML ice core δ^{18}O record (EPICA Community Members, 2006).

East Asia. In the record of Dongyuan Lake in Southern Taiwan (22°10′N, 120°50′E), the burial rate of organic matter reflected a generally humid period during the MI and a relatively drying transition that occurred at around 16.0 ka BP (Fig. 6e; Ding et al., 2016).

In a large-scale comparison, the records from the North Western Pacific Warm Pool and the South China Sea all show a sudden increase of terrigenous input from the Indochina Peninsula at around 17.5 ka BP (Fig. 6f and g; Huang et al., 2019; Li et al., 2019), which reflects enhanced regional rainfall as in the DN-1 core. However, the stalagmite record from the middle Yangtze region exhibits a change opposite to that of the DN-1 core, showing a slight rainfall decrease during 17.5–16.4 ka BP (Fig. 6b; Zhang et al., 2018). In North China, the ^{10}Be record from the Chinese Loess Plateau indicates a stable drying climate during the first stage of the MI (17.5–16.0 ka BP) (Fig. 6a; Zhou et al., 2012). As for the wet-dry transition process at the middle of the MI (16.0 ka BP), it is recorded in the sedimentary archives from the North Western Pacific Warm Pool and the southern EASM (Fig. 6f and g; Huang et al., 2019; Li et al., 2019). This change is the inverse of the record from the South Western Pacific Warm Pool (Fig. 6h; Muller et al., 2012). However, the stalagmite record in the middle Yangtze region shows that the last stage of the MI is an overall wet period, without an apparent wet-dry transition (Fig. 6b; Zhang et al., 2018). The ^{10}Be activities of the Chinese Loess Plateau indicate an overall arid environment in North China during the last stage of the MI (16.0–14.5 ka BP) (Fig. 6a; Zhou et al., 2012). Collectively, the wet-dry transition signal during the MI is strong in the lower latitude records from the West Pacific Warm Pool and the southern EASM but virtually absent in the higher latitude records from the middle Yangtze region and North China. Compared with the hydrological transition at the mid-MI being absent in the mid-latitude (30–40°N) EASM region, the dry-wet or wet-dry transition phenomena is recorded by the records in the mid-low latitudes of the Americas (Peterson et al., 2000; Broecker and Putnam, 2012). To sum up, the rainfall variation in the ASM region exhibits a strong response to the beginning of the MI, and the hydrological shift in the mid-MI had unique regional characteristics.

The El Niño-Southern Oscillation (ENSO) has been proposed to strongly influence the rainfall of the EASM area. Zhang (2001) observed that the middle Yangtze region experience intensive droughts during the La Niña phase, while rainfall in North China and the Indian monsoon region increase. In contrast, under the El Niño phase, the middle Yangtze region has heavy rain, while rainfall in North China and the Indian monsoon region decrease simultaneously. The observed phase relation between ENSO and precipitation in the middle Yangtze region and North China has been found in the geological records from the Holocene (Xie et al., 2013; Rao et al., 2016; Zhu et al., 2017; Wang et al., 2018). However, during the MI, although the model and geological records indicate that ENSO is in El Niño-like phase (Fig. 6i; Liu et al., 2014; Koutavas and Joanides, 2012), the rainfall in the middle Yangtze region shows a slight weakening (Fig. 6b). There is no apparent change in the rain in North China (Fig. 6a). The rainfall in the Indochina Peninsula increases first and then decreases abruptly (Fig. 6f and g). This regional difference suggests that ENSO is not the main controlling factor of rainfall distribution in the EASM region during the MI.

To resolve the atmospheric mechanism hidden in the above records, it is necessary to refer to a detailed relation between rainfall and atmospheric activities in observed and simulated studies. According to the regional characteristics of precipitation in the ASM region (Ding and Chan, 2005), the first monsoon rainfall peak on the Indochina Peninsula appears in May for the coverage of the ITCZ. From mid-May to mid-June, with the eastward advance of the Westerlies or the eastward shift of the West Pacific Subtropical High, rainfall in the south of EASM peaks, corresponding to the

arrival of the pre-Meiyu stage. Around mid-June, the rainfall peak appears in the middle Yangtze region due to the northward repositioning of the Westerlies, indicating the initiation of the Meiyu stage. Meanwhile, the ITCZ shows significant northward movement due to the eastward advance and northward shift of the Westerlies. In the simulation studies (Chiang et al., 2017, 2019; Zhang et al., 2018), cooling during the last deglaciation caused by the low North Hemisphere summer insolation phase of precession or by a large input of glacial meltwater in the North Atlantic Ocean would have cooled the entire Northern Hemisphere and would have been specially weighted towards higher latitudes. Therefore, the equator-to-pole temperature gradient is altered and causes a prolonged residence time of the Westerlies over the mid-south EASM. This would have increased the duration of pre-Meiyu and Meiyu stages of the ESAM, resulting in more rainfall in the southern EASM region and the middle Yangtze region. Moreover, the temperature gradient change between the Northern and Southern Hemispheres has frequently been considered to be the cause of the southward shift of the ITCZ (Chiang and Friedman, 2012).

Based on the observed and simulated results, the atmospheric activity in the ASM during the MI can be inferred from the distribution of rainfall. During 20.0–17.5 ka BP, the duration of the Westerlies in the mid-south of the EASM was longer due to the low Northern Hemisphere summer insolation phase of precession (Fig. 6j; Laskar et al., 2004), leading to extended pre-Meiyu and Meiyu stages, which caused a larger rainfall in the mid-south EASM. During 17.5–16.0 ka BP, the duration of Westerlies in the mid-south EASM was still longer, but weighted towards the southern EASM. This feature might be caused by the intensive cooling event induced by the large input of glacial meltwater in the North Atlantic Ocean, although the North Hemisphere summer insolation is relatively high during 17.5–16.0 ka BP (Fig. 6j; Laskar et al., 2004). Therefore, the records of DN-1 and the stalagmite in the middle Yangtze Region both indicate a wet climate during 17.5–16.0 ka BP, but show a contrary variation trend with each other (Fig. 6b, c, d). At around 17.5 ka BP, the rainfall on the Indochina Peninsula also increased, which might be induced by the longer residence time of the ITCZ over this area as the slowdown of the AMOC caused an ITCZ bias towards the Southern Hemisphere (Fig. 6a, b, c; Broecker and Putnam, 2012; Hodell et al., 2017).

The absence of a wet-dry transition in the mid-latitude area of the EASM during the MI might be due to the decoupling of the ITCZ and the Westerlies. According to the evolution of the EASM (Ding and Chan, 2005), during the early April–May stage of monsoon formation, the Tibetan Plateau high-pressure zone changed into a low-pressure zone due to seasonal heating from increased insolation, while oceans at the same longitude in the Southern Hemisphere show the opposite change. This process would induce the early formation of the ITCZ over the West Pacific Warm Pool. However, the Tibetan Plateau experienced cooling events due to the slowdown of AMOC during the MI (Opitz et al., 2015). In contrast, the SST of the South Hemisphere increased rapidly during the MI and reached its highest values after 16.0 ka BP (Fig. 6k; EPICA Community Members, 2006; Calvo et al., 2007). Therefore, the greater temperature gradient might have resulted in a slower process of pressure transition between the Tibetan Plateau and the ocean of the Southern Hemisphere and consequently delayed the early formation of the ITCZ in the Northern Hemisphere. This difference could be confirmed by the reverse phase observed between the records of the Western Pacific Warm Pool in the Northern and Southern Hemispheres (Fig. 6g and h; Muller et al., 2012; Huang et al., 2019). While the formation of the ITCZ was delayed, the overhead sunlight point moved northward, which would have promoted a rapid northward movement of the ITCZ after its formation. Therefore, the wet-dry transition phenomenon had a strong impact on the Indochina Peninsula and the southern EASM at the onset of the delay of the ITCZ but disappeared in the mid-Yangtze region and North China.

Collectively, the hydrological changes in the Asian Summer Monsoon region during the MI indicate that the second southward movement of the ITCZ is a seasonal delayed process that is caused by the strengthening of the temperature gradient between the Southern Hemisphere Ocean and the Tibetan Plateau. Therefore, it is necessary to consider the coupling situation between the ITCZ and the Westerly jet caused by the interhemispheric temperature gradient when considering the causes of the EASM rainfall variation in the past or future.

5. Conclusion

The CPI values and carbon isotope ratios of *n*-alkanes and elemental and isotopic composition of bulk organic matter of the DN-1 core reveal evidence of hydrological transitions at 17.5 ka BP and 16.0 ka BP in South China. The hydrological transition at 17.5 ka BP coincides with the start of the shutdown of AMOC, which might reflect the synchronous southward movement of the ITCZ and the Westerly jet caused by the cooling of the Northern Hemisphere. The hydrological transition at the mid-MI (16.5–16.0 ka BP) was strong in the lower latitude area but weak in the higher latitude area of the ASM, corresponding to the rapid SST increase in the Southern Hemisphere. This feature indicates a decoupling of the ITCZ and Westerly jet caused by the delayed formation of the ITCZ due to the warming of the Southern Hemisphere. This study not only provides evidence that supports a shift of the ITCZ during the middle of the MI caused by the warming of the Southern Hemisphere, but also emphasizes the importance of the coupling between the Westerly jet and the ITCZ to the rainfall of the ASM region.

Declaration of competing interest

The authors declare that they have no known competing financial interests or personal relationships that could have appeared to influence the work reported in this paper.

Acknowledgments

We gratefully acknowledge the Natural Science Foundation of China (Grant No. 41991252, 41876058) to JH, (U20A2094, 41877317) to XH, Strategic Priority Research Program of Chinese Academy of Sciences (No. XDB26000000), and Natural Science Foundation of China (No. 41877436) to SJ, the Earmarked Foundation of the State Key Laboratory of Organic Geochemistry (SKLOG 2020-3) and the Key Special Project for Introduced Talents Team of Southern Marine Science and Engineering Guangdong Laboratory (Guangzhou) (No. GML2019ZD0308) to JH. Prof. Philip A. Meyers from the University of Michigan is thanked for language editing and comments. The two anonymous reviewers and Dr. Patrick Rioual are acknowledged for their suggestions and comments to improve this manuscript.

Author contributions

JH, WW, PP and XH designed the study. JH and JS collected samples. BZ and JS performed analyses. BZ, XH and JH analyzed the data. BZ, XH and JH wrote the manuscript with contributions from all co-authors.

Appendix A. Supplementary data

Supplementary data to this article can be found online at https://doi.org/10.1016/j.quascirev.2021.107075.

References

Almquist, H., Dieffenbacher-Krall, A.C., Flanagan-Brown, R., Sanger, D., 2001. The Holocene record of lake levels of Mansell Pond, central Maine, USA. Holocene 11, 189–201.

Asmerom, Y., Polyak, V.J., Lachniet, M.S., 2017. Extrapolar climate reversal during the last deglaciation. Sci. Rep. 7, 7157.

Bi, X., Sheng, G., Liu, X., Li, C., Fu, J., 2005. Molecular and carbon and hydrogen isotopic composition of *n*-alkanes in plant leaf waxes. Org. Geochem. 36, 1405–1417.

Blaauw, M., Christen, J.A., 2011. Flexible paleoclimate age-depth models using an autoregressive gamma process. Bayesian Anal 6, 457–474.

Bray, E.E., Evans, E.D., 1961. Distribution of *n*-paraffins as a clue to recognition of source beds. Geochem. Cosmochim. Acta 22, 2–15.

Broecker, W., Putnam, A.E., 2012. How did the hydrologic cycle respond to the two-phase mystery interval? Quat. Sci. Rev. 57, 17–25.

Bush, R.T., Mcinerney, F.A., 2013. Leaf wax *n*-alkane distributions in and across modern plants: implications for paleoecology and chemotaxonomy. Geochem. Cosmochim. Acta 117, 161–179.

Cacho, I., Grimalt, J.O., Canals, M., Sbaffi, L., Shackleton, N.J., Schönfeld, J., Zahn, R., 2001. Variability of the western Mediterranean Sea surface temperature during the last 25,000 years and its connection with the Northern Hemisphere climatic changes. Paleoceanography 16, 40–52.

Calvo, E., Pelejero, C., De Deckker, P., Logan, G.A., 2007. Antarctic deglacial pattern in a 30 kyr record of sea surface temperature offshore South Australia. Geophys. Res. Lett. 34, L13707.

Chambers, F.M., Booth, R.K., De Vleeschouwer, F., Lamentowicz, M., Le Roux, G., Mauquoy, D., Nichols, J.E., Van Geel, B., 2012. Development and refinement of proxy-climate indicators from peats. Quat. Int. 268, 21–33.

Chen, L., Zhou, W., Zhang, Y., Zheng, Y., Huang, X., 2020. Postglacial floral and climate changes in southeastern China recorded by distributions of *n*-alkan-2-ones in the Dahu sediment-peat sequence. Palaeogeogr. Palaeocl. 538, 109448.

Chiang, J.C., Friedman, A.R., 2012. Extratropical cooling, interhemispheric thermal gradients, and tropical climate change. Annu. Rev. Earth Planet Sci. 40, 383–412.

Chiang, J.C., Fung, I.Y., Wu, C.H., Cai, Y., Edman, J.P., Liu, Y., Day, J.A., Bhattacharya, T., Mondal, Y., Labrousse, C.A., 2015. Role of seasonal transitions and westerly jets in East Asian paleoclimate. Quat. Sci. Rev. 108, 111–129.

Chiang, J., Swenson, L., Kong, W., 2017. Role of seasonal transitions and the westerlies in the interannual variability of the East Asian summer monsoon precipitation. Geophys. Res. Lett. 44, 3788–3795.

Chiang, J.C., Fischer, J., Kong, W., Herman, M.J., 2019. Intensification of the pre-Meiyu rainband in the late 21st century. Geophys. Res. Lett. 46, 7536–7545.

Chikaraishi, Y., Naraoka, H., 2003. Compound-specific δD–$\delta^{13}C$ analyses of *n*-alkanes extracted from terrestrial and aquatic plants. Phytochemistry 63, 361–371.

Chu, G., Sun, Q., Zhu, Q., Shan, Y., Shang, W., Ling, Y., Su, Y., Xie, M., Wang, X., Liu, J., 2017. The role of the Asian winter monsoon in the rapid propagation of abrupt climate changes during the last deglaciation. Quat. Sci. Rev. 177, 120–129.

Denton, G.H., 2006. The mystery interval 17.5 to 14.5 kyrs ago. PAGES News Letter 14, 14–16.

Diefendorf, A.F., Freimuth, E.J., 2017. Extracting the most from terrestrial plant-derived *n*-alkyl lipids and their carbon isotopes from the sedimentary record: a review. Org. Geochem. 103, 1–21.

Ding, Y.H., Chan, J.C., 2005. The East Asian summer monsoon: an overview. Meteorol. Atmos. Phys. 89, 117–142.

Ding, X., Zheng, L., Li, D., Yang, T.-N., Lee, T.-Q., Kao, S.-J., 2016. Lacustrine record of centennial-and millennial-scale rainfall variability of the East Asian summer monsoon during the last deglaciation: multi-proxy evidence from Taiwan. Palaeogeogr. Palaeocl. 450, 38–49.

Dong, X., Anderson, N.J., Yang, X., Chen, X., Shen, J., 2012. Carbon burial by shallow lakes on the Yangtze floodplain and its relevance to regional carbon sequestration. Global Change Biol. 18, 2205–2217.

EPICA Community Members, 2006. One-to-one coupling of glacial climate variability in Greenland and Antarctica. Nature 444, 195–198.

Farquhar, G.D., Ehleringer, J.R., Hubick, K.T., 1989. Carbon isotope discrimination and photosynthesis. Annu. Rev. Plant Biol. 40, 503–537.

Fenner, N., Freeman, C., 2020. Woody litter protects peat carbon stocks during drought. Nat. Clim. Change 10, 363–369.

Ficken, K.J., Li, B., Swain, D., Eglinton, G., 2000. An *n*-alkane proxy for the sedimentary input of submerged/floating freshwater aquatic macrophytes. Org. Geochem. 31, 745–749.

Finlay, J.C., Kendall, C., 2007. Stable isotope tracing of temporal and spatial variability in organic matter sources to freshwater ecosystems. In: Michener, R., Lajtha, K. (Eds.), Stable Isotopes in Ecology and Environmental Science, second ed. Wiley-Blackwell, pp. 283–333.

Freeman, K.H., Pancost, R.D., 2014. Biomarkers for terrestrial plants and climate. Treatise on Geochemistry, second ed., pp. 395–416

Han, L., Li, T., Cheng, H., Edwards, R.L., Shen, C., Li, H., Huang, C., Li, J., Yuan, N., Wang, H., Zhang, T., Zhao, X., 2016. Potential influence of temperature changes in the Southern Hemisphere on the evolution of the Asian summer monsoon during the last glacial period. Quat. Int. 392, 239–250.

Hedges, J., Oades, J., 1997. Comparative organic geochemistries of soils and marine sediments. Org. Geochem. 27, 319–361.

Hodell, D.A., Nicholl, J.A., Bontognali, T.R., Danino, S., Dorador, J., Dowdeswell, J.A., Einsle, J., Kuhlmann, H., Martrat, B., Mleneck-Vautravers, M.J., Rodriguez-Tovar, F.J., Röhl, U., 2017. Anatomy of Heinrich Layer 1 and its role in the last deglaciation. Paleoceanography 32, 284–303.

Hu, J., Peng, P., Jia, G., Mai, B., Zhang, G., 2006. Distribution and sources of organic carbon, nitrogen and their isotopes in sediments of the subtropical Pearl River estuary and adjacent shelf, Southern China. Mar. Chem. 98, 274–285.

Huang, X., Meyers, P.A., Xue, J., Zhang, Y., Wang, X., 2016. Paleoclimate significance of *n*-alkane molecular distributions and δ^2H values in surface peats across the monsoon region of China. Palaeogeogr. Palaeocl. 461, 77–86.

Huang, J., Wan, S., Li, A., Li, T., 2019. Two-phase structure of tropical hydroclimate during Heinrich Stadial 1 and its global implications. Quat. Sci. Rev. 222, 105900.

Jia, G., Bai, Y., Yang, X., Xie, L., Wei, G., Ouyang, T., Chu, G., Liu, Z., Peng, P., 2015. Biogeochemical evidence of Holocene East Asian summer and winter monsoon variability from a tropical maar lake in southern China. Quat. Sci. Rev. 111, 51–61.

Koutavas, A., Joanides, S., 2012. El niño–southern oscillation extrema in the Holocene and last glacial maximum. Paleoceanography 27, PA4208.

Kratz, T.K., DeWitt, C.B., 1986. Internal factors controlling peatland-lake ecosystem development. Ecology 67, 100–107.

Laskar, J., Robutel, P., Joutel, F., Gastineau, M., Correia, A.C.M., Levrard, B., 2004. A long-term numerical solution for the insolation quantities of the Earth. Astron. Astrophys. 428, 261–285.

Li, M., Ouyang, T., Tian, C., Zhu, Z., Peng, S., Tang, Z., Qiu, Y., Zhong, H., Peng, X., 2019. Sedimentary responses to the East Asian monsoon and sea level variations recorded in the northern South China Sea over the past 36 kyr. J. Asian Earth Sci. 171, 213–224.

Liu, Z., Lu, Z., Wen, X., Otto-Bliesner, B.L., Timmermann, A., Cobb, K.M., 2014. Evolution and forcing mechanisms of El Niño over the past 21,000 years. Nature 515, 550–553.

Loisel, J., Yu, Z., Beilman, D.W., Camill, P., Alm, J., Amesbury, M.J., Anderson, D., Andersson, S., Bochicchio, C., Barber, K., 2014. A database and synthesis of northern peatland soil properties and Holocene carbon and nitrogen accumulation. Holocene 24, 1028–1042.

Ma, T., Tarasov, P.E., Zheng, Z., Han, A., Huang, K., 2016. Pollen-and charcoal-based evidence for climatic and human impact on vegetation in the northern edge of Wuyi Mountains, China, during the last 8200 years. Holocene 26, 1616–1626.

Marzi, R., Torkelson, B., Olson, R., 1993. A revised carbon preference index. Org. Geochem. 20, 1303–1306.

Massa, C., Beilman, D.W., Nichols, J.E., Timm, O.E., 2021. Central Pacific hydroclimate over the last 45,000 years: molecular-isotopic evidence from leaf wax in a Hawai'i peatland. Quat. Sci. Rev. 253, 106744.

McGee, D., Moreno-Chamarro, E., Marshall, J., Galbraith, E.D., 2018. Western US lake expansions during heinrich stadials linked to pacific hadley circulation. Sci. Adv. 4, eaav0118.

McManus, J.F., Francois, R., Gherardi, J.-M., Keigwin, L.D., Brown-Leger, S., 2004. Collapse and rapid resumption of Atlantic meridional circulation linked to deglacial climate changes. Nature 428, 834–837.

Meyers, P.A., 2003. Applications of organic geochemistry to paleolimnological reconstructions: a summary of examples from the Laurentian Great Lakes. Org. Geochem. 34, 261–289.

Meyers, P.A., Ishiwatari, R., 1993. The early diagenesis of organic matter in lacustrine sediments. In: Engels, M.H., Macko, S.A. (Eds.), Organic Geochemistry: Principles and Applications. Plenum Press, New York, pp. 185–209.

Meyers, P.A., Lallier-Vergès, E., 1999. Lacustrine sedimentary organic matter records of Late Quaternary paleoclimates. J. Paleolimnol. 21, 345–372.

Mook, W., Bommerson, J., Staverman, W., 1974. Carbon isotope fractionation between dissolved bicarbonate and gaseous carbon dioxide. Earth Planet Sci. Lett. 22, 169–176.

Muller, J., McManus, J.F., Oppo, D.W., Francois, R., 2012. Strengthening of the northeast monsoon over the flores sea, Indonesia, at the time of heinrich event 1. Geology 40, 635–638.

Naafs, B., Inglis, G., Blewett, J., McClymont, E., Lauretano, V., Xie, S., Evershed, R., Pancost, R., 2019. The potential of biomarker proxies to trace climate, vegetation, and biogeochemical processes in peat: a review. Global Planet. Change 179, 57–79.

Newby, P.E., Killoran, P., Waldorf, M.R., Shuman, B.N., Webb, R.S., Webb III, T., 2000. 14,000 years of sediment, vegetation, and water-level changes at the Makepeace Cedar Swamp, southeastern Massachusetts. Quat. Res. 53, 352–368.

Nichols, J.E., Booth, R.K., Jackson, S.T., Pendall, E.G., Huang, Y., 2006. Paleohydrologic reconstruction based on *n*-alkane distributions in ombrotrophic peat. Org. Geochem. 37, 1505–1513.

Opitz, S., Zhang, C., Herzschuh, U., Mischke, S., 2015. Climate variability on the south-eastern Tibetan Plateau since the Lateglacial based on a multiproxy approach from Lake Naleng–comparing pollen and non-pollen signals. Quat. Sci. Rev. 115, 112–122.

Peterse, F., Prins, M.A., Beets, C.J., Troelstra, S.R., Zheng, H., Gu, Z., Schouten, S., Sinninghe Damsté, J.S., 2011. Decoupled warming and monsoon precipitation in East Asia over the last deglaciation. Earth Planet Sci. Lett. 301, 256–264.

Peterson, L.C., Haug, G.H., Hughen, K.A., Röhl, U., 2000. Rapid changes in the hydrologic cycle of the tropical Atlantic during the last glacial. Science 290, 1947–1951.

R Core Team, 2020. R: A Language and Environment for Statistical Computing. R Foundation for Statistical Computing, Vienna, Austria. http://www.r-project.

org/.
Rao, Z., Li, Y., Zhang, J., Jia, G., Chen, F., 2016. Investigating the long-term palaeoclimatic controls on the δD and $\delta^{18}O$ of precipitation during the Holocene in the Indian and East Asian monsoonal regions. Earth Sci. Rev. 159, 292–305.
Reimer, P.J., Bard, E., Bayliss, A., Beck, J.W., Blackwell, P.G., Ramsey, C.B., Buck, C.E., Cheng, H., Edwards, R.L., Friedrich, M., 2013. IntCal13 and Marine 13 radiocarbon age calibration curves 0–50,000 years cal BP. Radiocarbon 55, 1869–1887.
Schellekens, J., Buurman, P., 2011. *n*-Alkane distributions as palaeoclimatic proxies in ombrotrophic peat: the role of decomposition and dominant vegetation. Geoderma 164, 112–121.
Shakun, J.D., Clark, P.U., He, F., Marcott, S.A., Mix, A.C., Liu, Z., Otto-Bliesner, B., Schmittner, A., Bard, E., 2012. Global warming preceded by increasing carbon dioxide concentrations during the last deglaciation. Nature 484, 49–54.
Street, J.H., Anderson, R.S., Rosenbauer, R.J., Paytan, A., 2013. *n*-Alkane evidence for the onset of wetter conditions in the Sierra Nevada, California (USA) at the mid-late Holocene transition, ~ 3.0 ka. Quat. Res. 79, 14–23.
Thorson, R.M., Webb, R.S., 1991. Postglacial history of a cedar swamp in southeastern Connecticut. J. Paleolimnol. 6, 17–35.
Tipple, B.J., Pagani, M., 2013. Environmental control on eastern broadleaf forest species' leaf wax distributions and D/H ratios. Geochem. Cosmochim. Acta 111, 64–77.
Toggweiler, J., 2009. Shifting westerlies. Science 323, 1434–1435.
van der Valk, A., 2012. The Biology of Freshwater Wetlands. Oxford University Press.
Wan, R., Wang, T., Wu, G., 2008. Temporal variations of the spring persistent rains and South China Sea sub-high and their correlations to the circulation and precipitation of the East Asian Summer Monsoon. J. Meteorol. Res. 22, 530–537.
Wan, R., Zhao, B., Wu, G., 2009. New evidences on the climatic causes of the formation of the spring persistent rains over south-eastern China. Adv. Atmos. Sci. 26, 1081–1087.
Wang, G., Li, J., Liu, X., Li, X., 2013. Variations in carbon isotope ratios of plants across a temperature gradient along the 400 mm isoline of mean annual precipitation in north China and their relevance to paleovegetation reconstruction. Quat. Sci. Rev. 63, 83–90.
Wang, C., Bendle, J.A., Zhang, H., Yang, Y., Liu, D., Huang, J., Cui, J., Xie, S., 2018. Holocene temperature and hydrological changes reconstructed by bacterial 3-hydroxy fatty acids in a stalagmite from central China. Quat. Sci. Rev. 192, 97–105.
Wei, Z., Zhong, W., Xue, J., Ouyang, J., Shang, S., Ye, S., Cao, J., Li, M., 2020. Late Quaternary East Asian summer monsoon variability deduced from lacustrine mineral magnetic records of Dahu Swamp, southern China. Palaeogeogr. Palaeocl. 35, e2019PA003796.
Xie, S., Nott, C.J., Avsejs, L.A., Maddy, D., Chambers, F.M., Evershed, R.P., 2004. Molecular and isotopic stratigraphy in an ombrotrophic mire for paleoclimate reconstruction. Geochem. Cosmochim. Acta 68, 2849–2862.
Xie, S., Pancost, R.D., Huang, X., Jiao, D., Lu, L., Huang, J., Yang, F., Evershed, R.P., 2007. Molecular and isotopic evidence for episodic environmental change across the Permo/Triassic boundary at Meishan in South China. Global Planet. Change 55, 56–65.
Xie, S., Evershed, R.P., Huang, X., Zhu, Z., Pancost, R.D., Meyers, P.A., Gong, L., Hu, C., Huang, J., Zhang, S., Gu, Y., Zhu, J., 2013. Concordant monsoon-driven postglacial hydrological changes in peat and stalagmite records and their impacts on prehistoric cultures in central China. Geology 41, 827–830.
Yamoah, K.K., Chabangborn, A., Chawchai, S., Väliranta, M., Wohlfarth, B., Smittenberg, R.H., 2016. Large variability in *n*-alkane $\delta^{13}C$ values in Lake Pa Kho (Thailand) driven by wetland wetness and aquatic productivity. Org. Geochem. 97, 53–60.
Yu, X., Chen, J., Zheng, Y., Zhong, W., Ouyang, Z., Zhou, W., 2020. Anti-phase variation of hydrology and in-phase carbon accumulations in two wetlands in southern and northern China since the last deglaciation. Front. Earth Sci. 8, 192.
Zhang, R., 2001. Relations of water vapor transport from Indian Monsoon with that over East Asia and the summer rainfall in China. Adv. Atmos. Sci. 18, 1005–1017.
Zhang, H., Griffiths, M.L., Chiang, J.C., Kong, W., Wu, S., Atwood, A., Huang, J., Cheng, H., Ning, Y., Xie, S., 2018. East Asian hydroclimate modulated by the position of the westerlies during Termination I. Science 362, 580–583.
Zhao, B., Zhang, Y., Huang, X., Qiu, R., Zhang, Z., Meyers, P.A., 2018. Comparison of *n*-alkane molecular, carbon and hydrogen isotope compositions of different types of plants in the Dajiuhu peatland, central China. Org. Geochem. 124, 1–11.
Zheng, Y., Zhou, W., Xie, S., Yu, X., 2009. A comparative study of *n*-alkane biomarker and pollen records: an example from southern China. Chin. Sci. Bull. 54, 1065–1072.
Zhong, W., Cao, J., Xue, J., Ouyang, J., 2015. Last deglacial and Holocene vegetation evolution and climate variability in the subalpine western Nanling Mountains in South China. Holocene 25, 1330–1340.
Zhou, W., Yu, X., Jull, A.T., Burr, G., Xiao, J., Lu, X., Xian, F., 2004. High-resolution evidence from southern China of an early Holocene optimum and a mid-Holocene dry event during the past 18,000 years. Quat. Res. 62, 39–48.
Zhou, W., Xie, S., Meyers, P.A., Zheng, Y., 2005. Reconstruction of late glacial and Holocene climate evolution in southern China from geolipids and pollen in the Dingnan peat sequence. Org. Geochem. 36, 1272–1284.
Zhou, W., Wang, H., Zhu, Y., Xian, F., Liu, Z., 2012. The geological record of "Mystery Interval" in the last 21 ka. J. Earth Environ. 3, 685–691 (in Chinese with English abstract).
Zhu, Z., Feinberg, J.M., Xie, S., Bourne, M.D., Huang, C., Hu, C., Cheng, H., 2017. Holocene ENSO-related cyclic storms recorded by magnetic minerals in speleothems of central China. Proc. Natl. Acad. Sci. U. S. A 114, 852–857.